NANO LETTERS
Letter
Cite This: Nano Lett. 2019, 19, 9084−9094
pubs.acs.org/NanoLett

Probing Charge Carrier Transport and Recombination Pathways in Monolayer MoS_2/WS_2 Heterojunction Photoelectrodes

Li Wang,[†] Muhammad Tahir,[‡] Hua Chen,[‡,§] and Justin B. Sambur*[,†,§]

[†]Department of Chemistry, [‡]Department of Physics, [§]School of Advanced Materials Discovery (SAMD), Colorado State University, Fort Collins, Colorado 80523, United States

Supporting Information

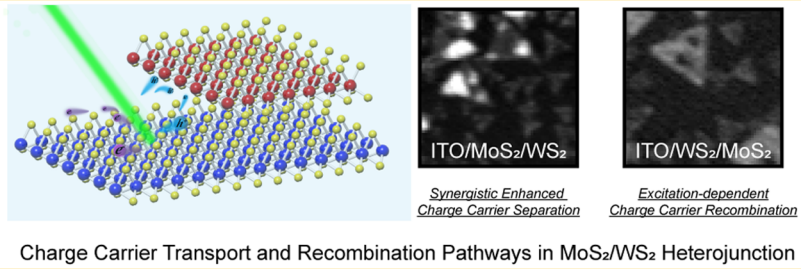

Charge Carrier Transport and Recombination Pathways in MoS_2/WS_2 Heterojunction

ABSTRACT: Monolayer heterojunctions such as MoS_2/WS_2 are attractive for solar energy conversion applications because the interfacial electric field spatially separates charge carriers in less than 100 fs. Photoelectrochemical cells represent an intriguing platform to collect the spatially separated carriers. However, the recombination, transport, and interfacial charge transfer processes that take place following the ultrafast charge separation step have not been investigated. Here we demonstrate novel charge recombination and transport pathways in monolayer MoS_2/WS_2 photoelectrochemical cells by spatially resolving the net collection of carriers (i.e., the photocurrent) at the single nanosheet level. We discovered an excitation-wavelength-dependent recombination pathway that depends on the heterojunction stacking configuration and the carrier generation profile in the heterostructure. Photocurrent mapping measurements revealed that charge transport occurs parallel to the layers over micrometer-scale distances even though the indium tin oxide electrode and liquid electrolyte provide efficient charge extraction pathways via intimate electron- and hole-selective contacts. Our results reveal how composition heterogeneity influences the performance of bulk heterojunction electrodes made from randomly oriented nanosheets and provide critical insight into the design of efficient heterojunction photoelectrodes for solar energy conversion applications.

KEYWORDS: *Monolayer photoelectrochemistry, transition metal dichalcogenides (TMDs), heterojunction, photoelectrochemical cell, photocurrent microscopy*

Transition metal dichalcogenides (TMDs) with the chemical formula MX_2, where M = Mo or W and X = S or Se, are layered materials that are held together by weak van der Waals interactions. The lack of covalent bonding between layers relaxes the lattice matching requirement for the layer-by-layer assembly of TMD heterojunctions.[1,2] This layer-by-layer stacking approach has been used to fabricate TMD heterojunction devices with tailored functional properties such as field-effect transistors,[3,4] light-emitting diodes,[5−7] photodetectors,[8,9] and photovoltaics.[10,11]

TMD heterojunctions such as MoS_2/WS_2 are particularly interesting for solar energy conversion applications. The physical coupling of TMDs with different electronic properties creates a driving force for charge separation at the heterojunction interface and facilitates charge transport to electrical contacts.[1,4,12] Charge transport is typically studied in solid-state device geometries, where the TMDs are stacked on top of each other and electrical contacts are deposited on the perimeter edges of the individual TMDs.[4,13] In this geometry, photogenerated carriers within the heterojunction region, or those carriers that can diffuse to the heterojunction region, may be separated efficiently. For MoS_2/WS_2 heterojunctions, this interlayer charge separation step produces electrons in MoS_2 and holes in WS_2. Following the interlayer charge separation step, electrons and holes must traverse long distances to reach electrical contacts. Charge transport takes place parallel to the layers across micron-scale distances instead of perpendicular to the layers across six atoms. Thus, solid-state devices with edge-on electrical contacts do not transport charge carriers across the atomically thin layers even though all carriers are produced at a charge-collecting interface. The long transport distances promote interlayer electron−hole recombination that ultimately limits the collection efficiency of photogenerated carriers.[10,13] It has been suggested that implementing perpendicular carrier transport pathways via the top and bottom carrier-selective contacts could improve heterojunction photoelectrode efficiency.[14]

Received: October 11, 2019
Revised: November 8, 2019
Published: November 18, 2019

DOI: 10.1021/acs.nanolett.9b04209
Nano Lett. 2019, 19, 9084−9094

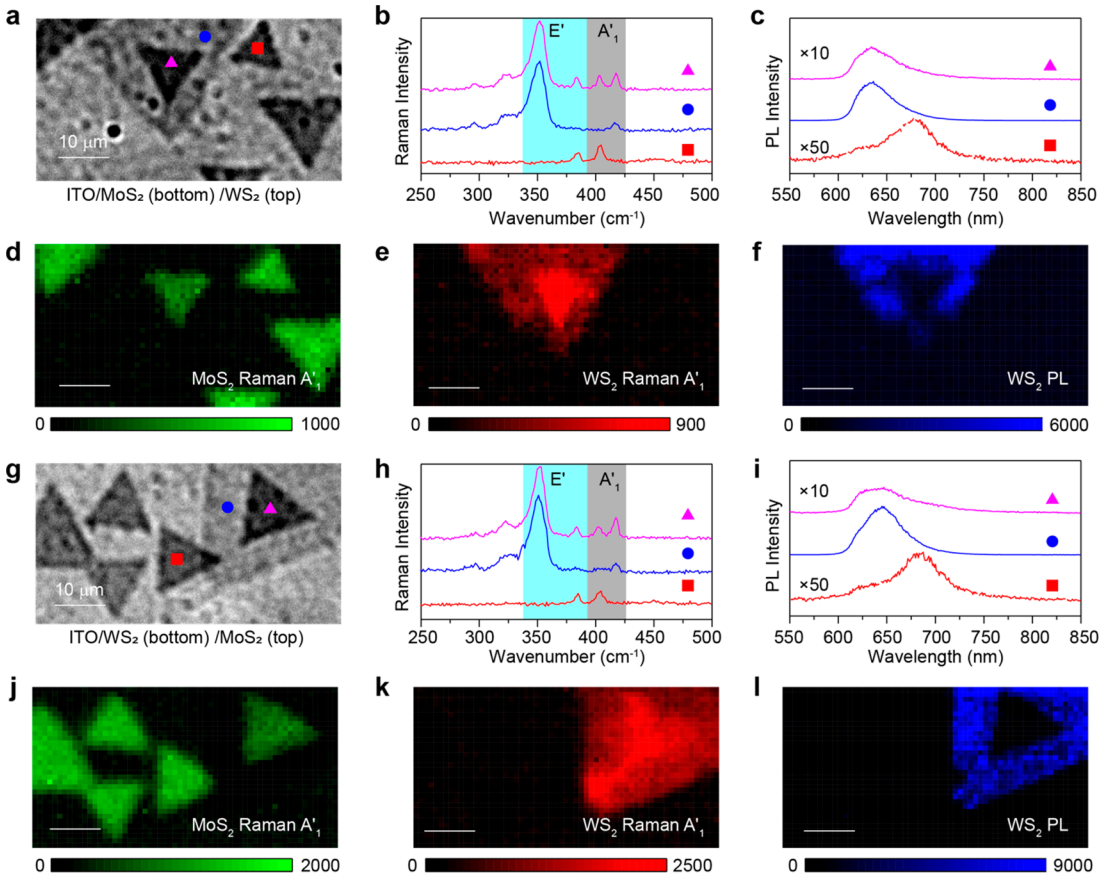

Figure 1. Raman and PL characterization of monolayer heterojunctions. (a) Bright-field optical transmission images of the ITO/MoS_2/WS_2 sample. (b) Raman spectra measured from the regions indicated in panel a. The gray and light blue shaded regions in panel b indicate the spectral regions of the out-of-plane A'_1 and in-plane E′ Raman modes. (c) PL spectra measured from the same regions in panel a. (d, e) Raman maps of the integrated peak intensity of the MoS_2 A'_1 mode centered at 402 cm^{-1} and the WS_2 A'_1 mode centered at 416 cm^{-1}. (f) PL map of the integrated PL intensity over the spectral range of 630−650 nm, corresponding to the WS_2 PL peak centered at 640 nm or 1.94 eV. Panels g−l are the same as that for panels a−f, but for the ITO/WS_2/MoS_2 stacking configuration. All spectra and maps were acquired in air, prior to photoelectrochemical measurements, using a focused 532 nm laser with a power density of 1.6 MW/cm^2. All scale bars are 10 μm.

Photoelectrochemical cells represent an alternative device geometry to study the underlying solar energy conversion processes in ultrathin materials. In the liquid junction geometry, the TMD heterojunction is deposited on a conducting electrode and immersed in a redox electrolyte. The solid electrode and redox electrolyte make intimate electrical contact to the TMD components and enable efficient perpendicular charge separation and transport pathways over large areas. We recently showed that this geometry promotes efficient extraction of photogenerated carriers in model photovoltaic systems, as evidenced by 3.7% external quantum efficiency (EQE) values over 1 cm^2 photoactive areas,[15] which is competitive with solid-state devices.[10,14] Electrochemical cells made from monolayer heterojunctions have been used to catalyze the hydrogen evolution reaction under dark conditions.[16−18] Photoelectrochemical cells made from multilayer-thick heterojunctions have been explored as water oxidation photoanode,[19,20] dye-sensitized solar cell counter electrodes,[21−23] and solar fuels photoelectrodes.[24−26] Multilayer-thick TMD films absorb more incident light than monolayer films. However, heterojunction films made from randomly oriented mixtures of different TMD nanosheets exhibit a wide variety of stacking configurations. It is unknown how different TMDs stacking orientations influence charge separation and transport in heterojunction photoelectrodes.

Several groups have studied charge separation and transport properties of TMD heterojunctions at open circuit and in solid-state devices.[10,13,14,27,28] Ultrafast spectroscopy measurements of TMDs have shown that the photoinduced interlayer charge transfer takes place on the femtosecond time scale,[29−33] but the charge transfer mechanism is not entirely understood. Chen et al. reported an interlayer charge transfer mechanism in MoS_2/WS_2 that proceeds via a hot exciton intermediate state.[30] An alternative process is fast interlayer energy transfer, as proposed by Eda and co-workers, where excitons in one TMDs (e.g., WS_2) excite higher-order excitons in the adjacent TMDs ($MoSe_2$).[34] Ceballos et al. reported a coherent charge transfer mechanism in trilayer TMD heterojunctions where photoexcited electrons in the top $MoSe_2$ layer transfer through a WS_2 middle layer to a MoS_2 underlayer in about one picosecond.[31] The above mechanisms were largely deduced from ultrafast optical spectroscopy measurements and theoretical calculations of TMD heterojunctions under open-circuit conditions. The relevant environment for optoelectronic and (photo)catalytic devices includes solid- or liquid-phase charge carrier-selective contacts to TMDs. An important open question in the field is to what extent do conformal contacts influence the charge recombination and transport pathways that ultimately lead to current flow in the external circuit. Little is known about charge separation and transport

DOI: 10.1021/acs.nanolett.9b04209
Nano Lett. 2019, 19, 9084−9094

in photoelectrochemical cells made from TMD heterojunctions.[33]

Here we investigated charge recombination and transport pathways in Schottky-type liquid junction solar cells made from vertically stacked MoS_2/WS_2 heterojunctions. We studied TMD heterojunctions in 1 M NaI electrolyte because hole-induced iodide oxidation by TMDs is one of the most efficient and chemically stable photoelectrochemical reactions.[35,36] Spatially resolved photocurrent measurements of different TMDs stacking configurations (ITO/MoS_2/WS_2 versus ITO/WS_2/MoS_2) under different illumination conditions revealed novel charge recombination and transport pathways in the monolayer heterojunction photoelectrodes. The ITO/MoS_2/WS_2 system exhibited a significant photocurrent enhancement effect under both 532 and 635 nm illumination. On the other hand, we observed excitation-wavelength-dependent charge separation and recombination pathways in the ITO/WS_2/MoS_2 system. Under 532 nm illumination that excites both TMDs, electrons in MoS_2 recombine with holes in WS_2. This interlayer recombination pathway is suppressed under MoS_2-selective (635 nm) conditions. Lastly, photocurrent mapping data and charge transport simulations showed that charge transport occurs parallel to the TMD layers via a diffusion mechanism even though the ITO electrode and liquid electrolyte provide facile perpendicular charge transport pathways.

Results and Discussion. *Optical Characterization of Monolayer Heterojunctions.* Monolayer MoS_2 and WS_2 samples were grown on sapphire substrates via a chemical vapor deposition process and transferred to indium doped tin oxide (ITO) substrates using poly(methyl methacrylate) (PMMA) stamps.[37] Two stacking configurations were prepared (ITO/MoS_2/WS_2 and ITO/WS_2/MoS_2) and annealed in a vacuum (ca. 10^{-3} mbar) at 120 °C for 6 h to the remove polymer residue from the mechanical transfer process and improve the interlayer coupling between the monolayers.[29] To minimize the influence of sample-to-sample heterogeneity, the heterojunctions were prepared from monolayers that were synthesized in the same batch and postannealed in a side-by-side fashion.

Raman and photoluminescence (PL) spectroscopy measurements were used to probe the interlayer charge transfer in the monolayer heterojunction under open-circuit conditions. Figure 1a,g shows representative bright-field optical transmission images of the ITO/MoS_2/WS_2 and ITO/WS_2/MoS_2 samples, respectively. Figure 1b shows Raman spectra that were measured from the focused laser positions in Figure 1a. The Raman spectra acquired from the isolated monolayer materials exhibit the characteristic out-of-plane (A'_1) and in-plane (E') modes of MoS_2 and WS_2. The 19 and 65 cm^{-1} splitting between the A'_1 and E' peaks indicates that the triangles are monolayer-thick MoS_2 and WS_2, respectively.[38,39] The large 20−30 μm triangles in Figure 1a,g are WS_2 monolayers, whereas the smaller 10 μm triangles are MoS_2 monolayers. MoS_2 absorbs more photons than WS_2 under white light illumination conditions, and therefore, the MoS_2 triangles exhibit dark contrast in transmission images. Raman spectra measured from the heterojunction region, corresponding to the sample region in Figure 1a,g, where the dark and light triangles spatially overlap, show no significant peak shifts for either stacking configuration.[29]

The PL spectra measured from both heterojunction stacking configurations exhibit significant intensity changes compared to the isolated materials. Isolated WS_2 exhibits an intense PL peak at around 640 nm, whereas MoS_2 exhibits a comparatively weaker PL peak at 684 nm and a smaller shoulder peak at 628 nm (Figure 1c, (i)), in agreement with literature.[29] The PL peaks at 640 nm (1.94 eV) and 684 nm (1.81 eV) correspond to the A exciton transition of the direct band gap monolayer WS_2 and MoS_2, respectively; the small shoulder peak in the MoS_2 spectrum corresponds to the indirect B exciton transition.[40] The PL spectrum from the photoexcited heterojunction region resembles that of the higher band gap WS_2. The weak MoS_2 PL peak at 684 nm is difficult to detect beneath the more intense WS_2 spectrum. Importantly, the PL intensity from the heterojunction region is an order of magnitude lower than that of isolated WS_2. The PL quenching behavior indicates interlayer charge transfer in the heterojunction region.[29]

Raman and PL mapping experiments further confirm that interlayer charge transfer occurs in both heterojunction stacking configurations under open-circuit conditions. Figure 1d−f (ITO/MoS_2/WS_2) and Figure 1j−l (ITO/WS_2/MoS_2) show the spatial distribution of the MoS_2 and WS_2 A'_1 Raman peak intensities and the integrated PL peak intensities. The out-of-plane A'_1 mode of WS_2 increases significantly (Figure 1e,k) in the heterojunction region, while the MoS_2 A'_1 intensity decreases slightly (Figure 1d,j) for both stacking configurations. Previous calculations of MoS_2/WS_2 heterojunctions showed that those peak intensity changes indicate that photoinduced interlayer charge transfer takes place between the physically coupled TMDs.[41,42] The peak intensity of the in-plane E' modes of MoS_2 and WS_2 show no significant intensity changes in both stacking configurations (Figure S1), presumably because the in-plane Raman modes of monolayer heterojunctions are typically less susceptible to changes in interlayer coupling.[38,43] On the other hand, the out-of-plane Raman modes are sensitive to the physical coupling between layers, and photoinduced interlayer photoexcited charge transfer occurs in strongly coupled MoS_2/WS_2 heterojunctions.[41,42] In summary, the PL spectra and spatially resolved Raman measurements indicate that interlayer charge transfer occurs for both monolayer heterojunction stacking configurations.

Probing Carrier Collection Efficiencies in Monolayer MoS_2/WS_2 Heterojunctions. Having established that interlayer charge transfer occurs in both heterojunction stacking configurations under open-circuit conditions, we probed the carrier collection efficiency of both heterojunctions using photocurrent microscopy measurements in ITO/TMDs/I^-, I_3^-/Pt photoelectrochemical cells. In a typical experiment, the electrochemical cell is mounted on the same inverted microscope that was used for Raman and PL microspectroscopy measurements. The sample stage moves the cell in 1 μm increments, while a tightly focused laser spot excites a 1 μm^2 area of the heterojunction working electrode. Supra-band gap illumination generates electron−hole pairs in the TMDs, and a potentiostat measures the photoinduced current response due to iodide oxidation. The charge transport pathways are as follows (Figure S2). Photogenerated holes are transported to the TMDs/electrolyte interface and oxidize I^- to I_2, which rapidly reacts with I^- to form I_3^-. Photogenerated electrons are transported to the TMDs/ITO contact and extracted to the external circuit. Photoelectrochemical microscopy measurements report on the net flow of charge through the entire nanosheet upon photoexciting a microscopic location within a

DOI: 10.1021/acs.nanolett.9b04209
Nano Lett. 2019, 19, 9084−9094

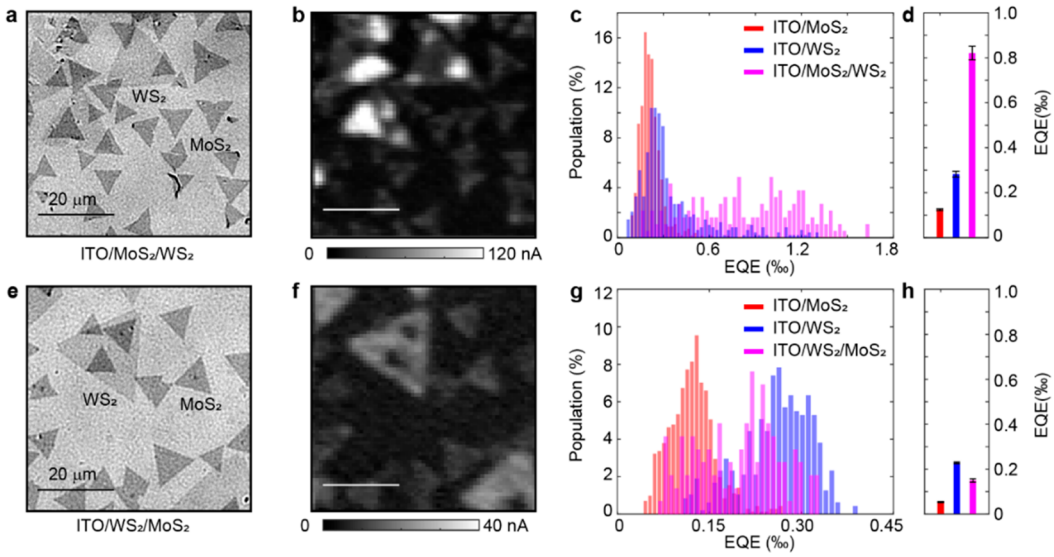

Figure 2. Scanning photoelectrochemical microscopy of monolayer heterojunctions under 532 nm excitation. (a) Optical transmission images and (b) photocurrent maps of ITO/MoS_2/WS_2 electrodes. Photocurrent maps were measured in 1 M NaI electrolyte at +0.5 V versus an Ag/AgI reference electrode using a 1.2 μm diameter and 532 nm laser spot (13.5 kW/cm^2). (c) EQE distributions from the photocurrent map in panel b. The distributions were determined using the detailed photocurrent mapping analyses procedures that are described in the Supporting Information, Note 1. (d) Average EQE values from the distributions in panel c, where the error bars represent the standard error of the mean. Panels e−h are the same as that for panels a−d, but for the ITO/WS_2/MoS_2 stacking orientation.

single nanosheet; the measurement does not report on the locations of hole-induced iodide oxidation reactions on the nanosheet surface. Our previous publications provide details on the experiment setup and image analysis procedures.[15,44]

Figure 2 shows representative optical transmission images and photocurrent maps of ITO/MoS_2/WS_2 and ITO/WS_2/MoS_2 electrodes at +0.5 V vs Ag/AgI and under 532 nm illumination conditions. The +0.5 V applied potential was chosen for photocurrent mapping experiments because (1) it is the most positive anodic bias that can be applied to the TMDs electrode without producing dark anodic currents due to iodide oxidation, and (2) it minimizes photocurrent transient effects that could influence the lock-in detected current; these lock-in detected currents represent the steady-state photocurrent response (Figure S3). Qualitative comparison of the transmission and photocurrent images in Figure 2a,b indicates that the largest photocurrents (bright pixels) stem from photoexcited ITO/MoS_2/WS_2 regions.

To quantitatively compare the photocurrent response from isolated MoS_2 and WS_2 to that of MoS_2/WS_2, we assign every pixel in the photocurrent map to photoexcited ITO, MoS_2, WS_2, or MoS_2/WS_2 regions using an image overlay procedure that is described in Figure S4 and Note 1. Figure 2c shows the distribution of external quantum efficiency (EQE) values, respectively, from photoexcited MoS_2, WS_2, and MoS_2/WS_2 regions of the sample in Figure 2a. The monochromatic external quantum efficiency is calculated according to EQE = i/qI_{inc}, where i is the photocurrent (A), q is the elementary charge (C), and I_{inc} is the incident 532 nm laser power (s^{-1}). The broad distribution of EQE values among the different regions are presumably due to heterogeneity among the nanosheets. Figure 2d shows that, on average, the ITO/MoS_2/WS_2 heterojunction region exhibits a significant synergistic enhancement effect over the isolated MoS_2 and WS_2 areas. Specifically, the EQE of ITO/MoS_2/WS_2 (0.8%) exceeds the sum of MoS_2 and WS_2 (0.4%). The enhancement behavior in Figure 2a−d was observed for different areas from the same cell as well as other cells (Figures S5 and S6), indicating that the synergistic enhancement effect is general for these ITO/MoS_2/WS_2 heterojunctions.

We attribute the photocurrent enhancement effect for ITO/MoS_2/WS_2 to an increase in the charge separation efficiency. This can be rationalized as follows: a general expression for photocurrent density of a photoelectrochemical cell, $J_{PEC} = J_{abs} \times \eta_{sep} \times \eta_{int}$, where J_{abs}, η_{sep}, and η_{int} are the absorbed photon flux, the efficiencies of charge separation, and interfacial charge transfer to redox species in the electrolyte, respectively.[45] The increase in EQE for ITO/MoS_2/WS_2 is likely not due to an increase in η_{int} because the catalytic properties likely do not change for the physically coupled TMDs, and we performed control measurements on the same batch of nanosheets that are located just microns apart. In addition, light absorption enhancement in the heterojunction also cannot account for the EQE enhancement because the absorption spectrum of the heterojunction is approximately the sum of the individual monolayers, and we observed that the EQE of ITO/MoS_2/WS_2 exceeds the sum of the monolayers by a factor of 2 (Note 2 and Figures S7 and S8). Thus, we attribute the increase in EQE to an increase in η_{sep} as a result of the conduction band level offset between WS_2 and MoS_2, as will be discussed below.

On the contrary, the ITO/WS_2/MoS_2 stacking orientation showed a significant photocurrent quenching effect under 532 nm laser illumination. The photocurrent map in Figure 2f shows that photoexcited heterojunction regions produce low photocurrents (dark pixels), which indicates that photoexcited carriers in the heterojunction mostly recombine and do not participate in the iodide oxidation reaction. We note that the photocurrent response from the ITO/WS_2/MoS_2 regions is not completely suppressed and is larger than that of bare ITO regions. Photocurrent maps from other electrochemical cells and sample regions show the same quenching behavior (Figure S9). The EQE distribution of the ITO/WS_2/MoS_2 is broad and exhibits two populations that overlap with ITO/MoS_2 and ITO/WS_2 (Figure 2g). Quantitative analysis of the ITO/WS_2/

DOI: 10.1021/acs.nanolett.9b04209
Nano Lett. 2019, 19, 9084−9094

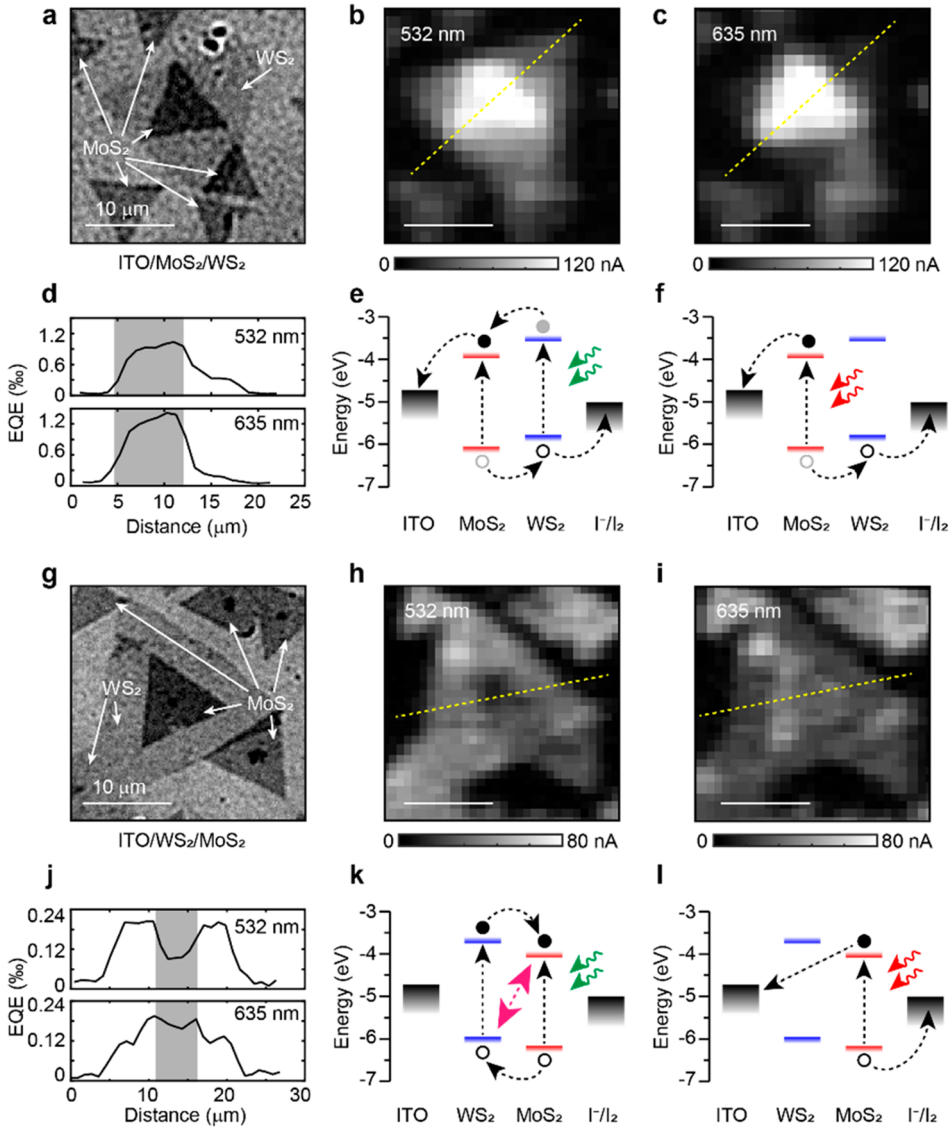

Figure 3. Charge carrier transport and recombination pathways under both green and red illumination conditions. (a) Optical transmission image of the ITO/MoS_2/WS_2 sample. (b, c) Photocurrent maps under (b) 13.5 kW/cm^2 532 nm laser excitation and (c) 5.7 kW/cm^2 635 nm laser excitation. The 532 and 635 nm laser spot diameters were 1.2 and 1.8 μm in diameter, respectively. The total number of incident photons per second was equal in red and green photocurrent mapping experiments. The photocurrent maps were measured in 1 M NaI electrolyte at +0.5 V versus an Ag/AgI reference electrode. For reference, the equilibrium potential for the I^-/I_2 redox couple is 0.63 V versus Ag/AgI. (d) EQE versus the distance line profile measured from the yellow lines in panels b and c. (e, f) Schematic energy level diagram and proposed charge recombination and transport pathways in the heterojunction region under green and red laser illumination, respectively. Panels g−l are the same as that of panels a−f, but for ITO/WS_2/MoS_2.

MoS_2 photocurrent map indicates that ITO/WS_2/MoS_2 does not exceed the sum of the isolated TMD components (Figure 2h). Similarly, the photocurrent quenching effect is likely not due to a small η_{int} (i.e., local differences in catalytic properties) because we performed control experiments on isolated materials and confirmed that both materials oxidize iodide. Instead, the photocurrent quenching effect should likely arise from the small η_{sep} as a result of physically coupling individual TMD components in the ITO/WS_2/MoS_2 stacking configuration.

Probing Charge Carrier Transport and Recombination Pathways in Two Heterojunctions. To understand the relationship between carrier generation, recombination, and transport in these MoS_2/WS_2 stacking configurations, we studied the photocurrent response under both 532 nm (green) and 635 nm (red) excitation conditions. The red laser preferably excites the low band gap MoS_2 material, whereas the green laser excites both materials (Figure S7). Figure 3b,h shows zoomed-in photocurrent maps of the ITO/MoS_2/WS_2 and ITO/WS_2/MoS_2 stacking configurations under 532 nm excitation (Figure S10 shows the whole photocurrent maps). We observed the same photocurrent enhancement and quenching behavior as shown in Figure 2. Then, we measured photocurrent maps of the same regions under 635 nm excitation (Figure 3c,i). The ITO/MoS_2/WS_2 sample showed the same photocurrent enhancement effect under 635 nm excitation (Figure 3c), indicating that photogenerated carriers in the MoS_2 are efficiently extracted from the bottom layer in the heterojunction. The line profiles in Figure 3d quantify the

DOI: 10.1021/acs.nanolett.9b04209
Nano Lett. 2019, 19, 9084−9094

photocurrent responses under different illumination conditions.

We observed a synergistic enhancement effect when MoS_2 and WS_2 are physically coupled, but only MoS_2 is photoexcited. Figure 3a,c shows that under MoS_2-selective excitation conditions, photoexcited MoS_2 in the ITO/MoS_2/WS_2 region produces a larger photocurrent than isolated MoS_2. The EQE of ITO/MoS_2/WS_2 is about 2.5 times larger than that of ITO/MoS_2 under 635 nm excitation conditions (Figure S11). Photogenerated carriers in MoS_2 are more efficiently separated if those carriers are produced in the heterojunction region than in the isolated region. In other words, η_{sep} is larger for photogenerated carriers in ITO/MoS_2/WS_2 than for ITO/MoS_2. We attribute the enhanced separation efficiency to a built-in electric field that promotes rapid hole transfer from the bottom MoS_2 layer to the top WS_2 layer.

Interestingly, we did not observe a significant photocurrent quenching effect for the ITO/WS_2/MoS_2 samples under 635 nm excitation conditions even though the same triangle exhibits a photocurrent quenching effect under 532 nm laser conditions (Figure 3i versus h). The line profiles in Figure 3j show that the photocurrent response in the heterojunction region under the 635 nm illumination condition increases compared to the 532 nm illumination condition. This observation does not depend on the order of the experiments; the results hold true whether the 532 nm map was performed before or after the 635 nm mapping experiment (Figure S10 versus Figure S12). We also note that the incident photons per second are equal in both experiments, and therefore the observation is not due to differences in carrier generation. In the ITO/WS_2/MoS_2 stacking configuration under MoS_2-selective illumination conditions, photogenerated electrons are transferred from the MoS_2 top layer to the ITO electrode through the WS_2 bottom layer. Ceballos et al. reported a similar, anomalous charge transport pathway in trilayer TMDs, where charge carriers flowed from a top $MoSe_2$ monolayer to a bottom MoS_2 monolayer without populating the middle WS_2 monolayer.[31]

We propose the following charge generation, recombination, and transport schemes to explain the photocurrent mapping data for both heterojunction configurations under green and red excitation conditions. Theoretical[12] and experimental[46] studies have shown that monolayer MoS_2 and WS_2 form a type-II energy band alignment where the conduction band minimum (CBM) of WS_2 is 0.35 eV above (or more negative on the electrochemical scale) the CBM of MoS_2, and the valence band maximum (VBM) of WS_2 is 0.39 eV above that of MoS_2. The type-II band alignment promotes electron transfer from WS_2 to MoS_2 and hole transfer from MoS_2 to WS_2.[12,33] For the ITO/MoS_2/WS_2 configuration, the type-II energy level alignment promotes electron and hole transport to the ITO and electrolyte contacts, respectively (Figure 3e). The charge transport pathway of photogenerated carriers in MoS_2 does not depend on the excitation wavelength (Figure 3f). The overall charge separation and transport efficiency of carriers in MoS_2 is enhanced significantly if those carriers are produced in the heterojunction region instead of an isolated MoS_2 region. The photocurrent enhancement effect for the ITO/MoS_2/WS_2 stacking configuration can be attributed to a rapid interlayer charge separation that produces spatially separated electrons and holes near hole-selective and electron-selective contacts.

For the ITO/WS_2/MoS_2 stacking configuration, the charge recombination and transport pathways critically depend on carrier generation in the TMDs. We observed a large photocurrent response upon exciting the heterojunction region with 635 nm light during a small photocurrent response when both TMDs were excited simultaneously with 532 nm light. Thus, charge carrier generation in both materials induces a recombination pathway that is not present under MoS_2-selective carrier generation conditions. This result suggests that electrons in the conduction band of MoS_2 recombine with holes in the valence band of WS_2, as shown in Figure 3k. In this scenario, green light generates excitons in both materials (vertical black arrows in Figure 3k). Next, interlayer charge transfer occurs on an ultrafast time scale (~50 fs).[29] Photogenerated electrons in the low-lying conduction band of MoS_2 recombine with valence band holes in WS_2 (pink arrow in Figure 3k). Photogenerated electrons in the low lying conduction band of MoS_2 recombine with valence band holes in WS_2 (pink arrow in Figure 3k) likely because (1) the spatially separated electrons and holes are not located near their respective carrier-selective contacts (i.e., ITO and electrolyte), and (2) the type-II energy level alignment imposes a potential energy barrier for electrons and holes to transfer into the ITO and electrolyte contacts, respectively. Alternatively, it is also possible that photogenerated holes in the top MoS_2 layer rapidly oxidize iodide to I_2 or I_3^-. Since there is an energy barrier for photogenerated electrons in MoS_2 to transfer to the bottom WS_2 layer, the photogenerated electrons could react with the surface adsorbed oxidized products (I_2 or I_3^-), leading to the photocurrent quenching behavior. Regardless of the underlying mechanism, a photogenerated hole population in the WS_2 bottom layer is apparently necessary to activate the interlayer recombination channel. Lee et al. proposed a similar interlayer charge recombination process to explain electron−hole recombination in solid-state MoS_2/WS_2 heterojunctions with lateral electrical contacts.[10] The authors proposed that interlayer charge recombination occurs through either a Shockley−Read−Hall or Langevin mechanism or a combination of both.

Figure 3l shows one possible charge separation and transport pathway for the ITO/WS_2/MoS_2 stacking configuration under 635 nm illumination conditions. In this scenario, electrons transfer from the MoS_2 top layer through the WS_2 bottom layer to the ITO electrode. Holes in MoS_2 transfer to the intimately coupled electrolyte contact. One could have expected a recombination pathway, where ultrafast interlayer hole transfer occurs first from the top MoS_2 layer to the bottom WS_2 layer (not illustrated in Figure 3i), and then interlayer electron−hole recombination occurs as shown in Figure 3k. While this recombination pathway could still take place in the system, our 635 nm photocurrent mapping measurements indicate the photogenerated hole transfer to the iodide electrolyte likely outcompetes interlayer hole transfer (followed by recombination). Finally, we note that the small photocurrent response from isolated WS_2 regions under 635 nm excitation (Figure 3i) is likely due to a minor overlap of the 635 ± 1 nm laser line (Figure S13) with the absorption onset of the WS_2 A-exciton peak (Figure S7). Thus, the 635 nm photocurrent mapping measurements may underestimate the true magnitude of the photocurrent response of the ITO/WS_2/MoS_2 heterojunction under MoS_2-selective conditions because the small photogenerated exciton population in the bottom WS_2 layer could induce the recombination pathway illustrated in Figure 3k. We addressed this issue by photoexciting the sample with 650 nm light from a white light source

DOI: 10.1021/acs.nanolett.9b04209
Nano Lett. 2019, 19, 9084−9094

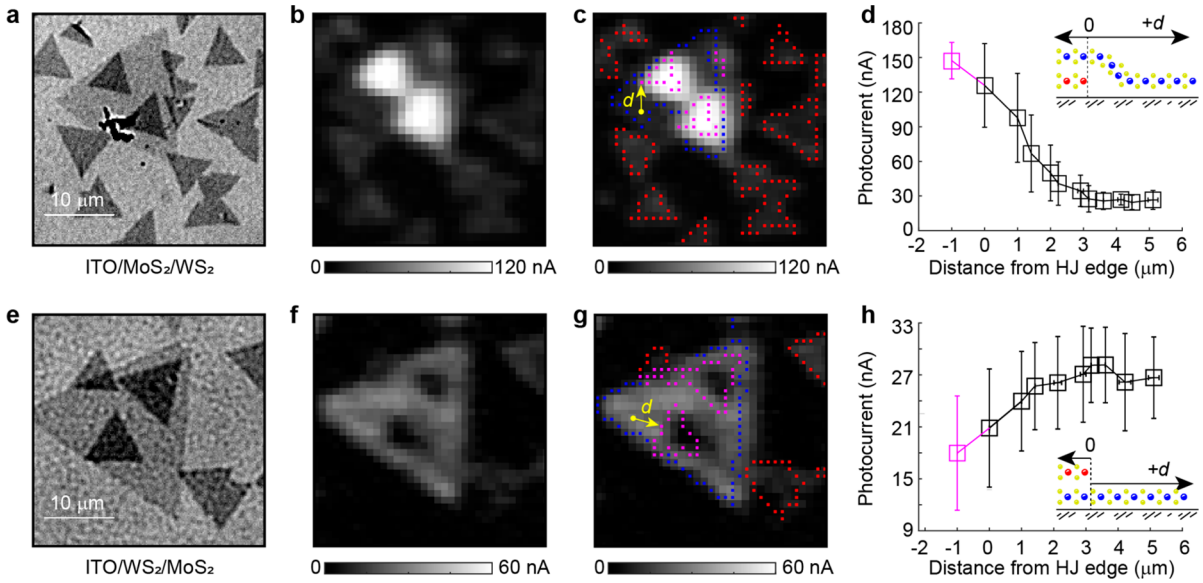

Figure 4. Probing lateral charge carrier transport in monolayer heterojunctions. (a) Optical transmission image of the ITO/MoS_2/WS_2 sample. (b) Photocurrent map of the area in panel a. (c) Same as panel b with the red, blue, and pink pixels representing MoS_2, WS_2, and heterojunction regions, respectively. Note 3 in the Supporting Information describes the pixel assignment procedure. (d) Photocurrent of WS_2 as a function of distance to the nearest heterojunction edge site (d). The data points represent the binned and average values from all pixels in the photocurrent map in panel b. The data does not include isolated WS_2 (i.e., material that is not connected to a MoS_2 triangle). The error bars represent the standard deviation of the values in that bin. Panels e−h are the same as that for panels a−d, but for the ITO/WS_2/MoS_2 stacking configuration. The arrow labeled "d" in panels c and g represents the vector from the photocurrent pixel to the nearest heterojunction edge site. The purple points in panels d and h represent the average photocurrent from 1 μm inside the heterojunction edge, or $-d$ values, as illustrated in the insets of panels d and h.

coupled to a monochromator (excitation profile shown in Figure S14), as will be discussed in the current−voltage measurements below.

While the photocurrent quenching result under 532 nm excitation conditions can be rationalized by the mechanism in Figure 3k, it is still surprising that electron−hole recombination occurs despite the fact that (1) there are parallel and perpendicular charge transport pathways for holes to reach the electrolyte, and (2) the applied potential generates a strong internal electric field that drives charge separation. One could have expected electrons and holes to transfer through the potential energy barriers imposed by the ultrathin TMDs, as in Figure 3i. Instead, the strong interlayer electronic coupling promotes ultrafast charge separation, followed by interlayer recombination. Importantly, our photocurrent microscopy approach revealed all of the above relationships between carrier generation, transport, and recombination on heterojunction samples that contained isolated TMDs attached directly to the heterojunction region. Photocurrent measurements of the isolated materials serve as key control experiments that rule out sample heterogeneity or batch-to-batch variations as possible contributing factors to the photocurrent mapping observations.

Lateral Charge Transport in Monolayer Heterojunctions under 532 nm Excitation. Spatially resolved photocurrent mapping measurements revealed that charge carriers flow parallel to the TMDs layers even though the ITO electrode and liquid electrolyte provide perpendicular charge transport pathways. We performed the following image analysis procedure to study parallel charge transport pathways. Figure 4b shows a photocurrent map of the ITO/MoS_2/WS_2 region in Figure 4a. Figure 4c shows the same data as in Figure 4b, but the perimeter edges of the MoS_2, WS_2, and MoS_2/WS_2 regions are highlighted with red, blue, and purple pixels, respectively. The detailed structural overlay procedures and additional control experiments are provided in the Supporting Information, Note 3. The bright contrast pixels in Figure 4c extend beyond the heterojunction boundary, and the dark contrast pixels in Figure 4g occur deeper within the heterojunction interior; the photocurrent enhancement and quenching effect extend beyond the physical size of the heterojunction triangle regions.

To quantitatively show how the heterojunction influences parallel charge transport, we extract the photocurrent value for all large WS_2 triangles that were physically coupled to a small MoS_2 triangle (i.e., blue pixels in Figure S15) and plotted those values versus distance of that WS_2 region to the nearest heterojunction edge site (nearest pink pixel in Figure 4c). The detailed image analysis procedure is provided in Supporting Information, Note 3. Figure 4d shows the photocurrent versus distance to the heterojunction edge (d) profile for the WS_2 triangle in Figure 4c. For large d values (>3 μm), photoexcited WS_2 produces a 30 nA photocurrent that is independent of d. Then, for $d < 3$ μm, the photocurrent increases monotonically with decreasing d and eventually exhibits a maximum inside the heterojunction region ($-d$ values). The photocurrent increase at small d values is likely not due to the diffraction-limited resolution of the experiment or a broad laser excitation spot because a line profile analysis of the laser reflection map (Figure S16 and detailed discussion in Note 4) shows a more abrupt transition across the heterojunction edge than the photocurrent profile in Figure 4d. In addition, control experiments of ITO/MoS_2 regions also showed an abrupt transition across the MoS_2 edge/ITO interface (Figure S16 and Note 4), indicating that the diffraction-limited resolution and light scattering cannot account entirely for the behavior

DOI: 10.1021/acs.nanolett.9b04209
Nano Lett. 2019, 19, 9084−9094

observed in Figure 4d. Instead, we conclude that photogenerated carriers in isolated WS_2 "feel" the heterojunction edge even though they are spatially separated by about 3 μm.

We performed the same analysis for the ITO/WS_2/MoS_2 stacking configuration (Figure 4e–h). For large d values (>3 μm), photoexcited WS_2 produces a 30 nA photocurrent that is independent of d, which is expectedly similar to the isolated material from the other stacking configuration (Figure 4d). The d-independent regions of both stacking configurations highlight the fact that the photoexcited WS_2 material far from the heterojunction region behaves like isolated WS_2 that is not physically coupled to MoS_2. However, for d < 3 μm, the photocurrent decreases monotonically with decreasing d in the ITO/WS_2/MoS_2 stacking configuration (Figure 4h). Again, photogenerated carriers in isolated WS_2 "feel" the heterojunction edge even though the carriers are generated several microns from the heterojunction region. We observed similar behavior for other regions in both electrochemical cells (Figure S17).

Here we discuss the possible mechanisms of the photocurrent versus distance behavior in Figure 4d,h. One possible mechanism for this parallel charge transport behavior is that carriers move in an electric field due to a drift mechanism. In this scenario, charge carriers are transported in an electric field that forms at the heterojunction edge and extends into the WS_2 monolayer. A similar mechanism has been used to explain charge recombination at step edges in bulk TMDs/iodide photoelectrochemical cells.[47,48] Howell et al. reported a similar effect at the edge sites in monolayer/multilayer MoS_2-based devices.[49] It is plausible that the drift mechanism occurs over micrometer-scale distances because Kelvin probe force microscopy (KPFM) experiments showed that the width of the parallel electric field region is about 3 μm.[50,51] However, those KPFM measurements were performed in air, and our measurements were performed in concentrated electrolyte solutions. Another possibility is that the charge carriers diffuse along a concentration gradient. In this scenario, the carrier concentration is high at the focused laser spot, and therefore, carriers diffuse from regions of high carrier concentration to low carrier concentration (i.e., toward the heterojunction edge).

To confirm the underlying mechanism of the parallel charge transport processes in these TMD heterojunctions, we performed charge transport simulations based on a simplified one-dimensional model (see Supporting Information, Note 5, for details), following standard practices in the field. Briefly, we solved Poisson's equation to determine the electric potential in the TMD heterojunction under dark equilibrium conditions. Those calculations showed that the thickness of the electric field region in WS_2 at the heterojunction interface is at most 30 nm, due to the strong screening by the 1 M NaI electrolyte and the ITO substrate in contact with the TMD layers. Since the photocurrent decay behavior occurs over a much longer length scale, the lateral electric field at the heterojunction interface likely does not contribute to the photocurrent versus distance behavior in Figure 4d,h. Simulations in the steady state under focused laser illumination show that the parallel charge transport process is driven by carrier diffusion along a concentration gradient from the point of generation (focused laser spot) to the heterojunction edge site. The micron-scale diffusion length is likely due to the relatively long exciton lifetime (typically over 100 ps) in the TMD layers.[52]

Current–Voltage Characteristics. To further confirm the charge carrier pathways proposed in Figure 3, the energetics of the TMDs/liquid electrolyte interface was studied using wavelength-dependent photocurrent versus applied potential (i-E) curves. We determined the photocurrent onset potential (E_{on}) from i-E data because E_{on} represents the minimum applied potential to separate charge in the photoexcited semiconductors.[53,54] In other words, we assume that i = 0 nA when $E = E_{on}$ because there is no electric field in the TMDs to drive charge separation. At this flatband condition, the applied potential is equal to the energy level difference between the Fermi level of the TMDs (E_F) and the electrochemical potential of the liquid electrolyte E^0 (I^-/I_2).[55] Since the solution potential does not change for the different stacking configurations and illumination conditions, we determine the Fermi level alignment of the isolated and heterojunction TMDs relative to the fixed solution potential.[56]

Figure 5 shows the i-E curves of the ITO/WS_2/MoS_2 and ITO/MoS_2/WS_2 samples under 532 nm (3.0 mW/cm^2) and

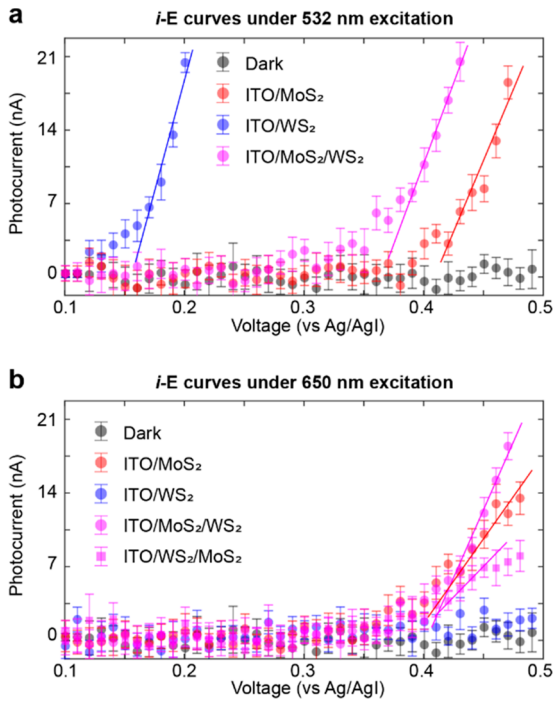

Figure 5. Wavelength-dependent photocurrent versus applied potential curves. (a) i-E data under 532 nm (3.0 mW/cm^2) and (b) 650 nm (2.4 mW/cm^2) illumination, respectively. The illumination spot size was 1.13 mm^2. The solid lines represent linear fits to the i-E data.

650 nm (2.4 mW/cm^2) illumination using a white light source coupled to a monochromator (1.13 mm^2 excitation area). While we sacrifice spatial resolution with this light source, the 650 nm illumination removes any possibility of photoexcitation of WS_2 (Figure S7). The i-E measurements were performed under chopped light conditions with a lock-in amplifier to detect small changes in the transient photocurrent response due to charge separation; the onset potential measured under steady-state illumination typically overestimates the minimum applied potential for charge separation.[57] For all materials and both excitation conditions, the photocurrent is approximately 0 nA at cathodic potentials (E < 0.10 V vs a Ag/AgI reference electrode) and then increases approximately linearly with

DOI: 10.1021/acs.nanolett.9b04209
Nano Lett. 2019, 19, 9084–9094

increasing anodic potentials. We attribute the linear *i-E* response to a linear electric potential profile in the TMDs, whose magnitude increases linearly with increasingly anodic potential, in agreement with literature.[10,15] We extract E_{on} by fitting the *i-E* response with a linear function and solving for *E* when $i = 0$ nA.

Under 532 nm excitation, the E_{on} for ITO/WS_2 is 0.25 V more negative than that of ITO/MoS_2 (Figure 5a, blue versus red traces). Since $E_F = E_{on} + E^0$ (I^-/I_2) and the solution potential does not change during these measurements, the more negative E_{on} value for WS_2 indicates that E_F of WS_2 is 0.25 V more negative on the electrochemical scale than MoS_2, which is consistent with literature.[12,58] Here we have assumed that the energy difference between the Fermi level and conduction band minimum is the same for both materials.[59] The E_{on} value of the ITO/MoS_2/WS_2 configuration under 532 nm illumination conditions lies between isolated ITO/MoS_2 and ITO/WS_2, which is in agreement with theoretical predictions that the Fermi level of the heterojunction is located between that of the isolated TMDs.[58] The ITO/WS_2/MoS_2 sample contained a large fraction of exposed WS_2 triangles that contribute to the photocurrent response under these large area excitation conditions, and therefore we were unable to measure the *i-E* response of pure ITO/WS_2/MoS_2 material. *i-E* measurements of ITO/WS_2/MoS_2 samples that contain some isolated WS_2 indicate that E_{on} is between ITO/MoS_2 and ITO/WS_2 under 532 nm illumination conditions, which further indicates that that the Fermi level of the heterojunction is located between that of the isolated TMDs (see discussion in Note 6, Supporting Information).

Surprisingly, under 650 nm illumination conditions, the E_{on} of ITO/WS_2/MoS_2 is nearly equivalent to ITO/MoS_2 (0.4 V in Figure 5b). This result supports the charge transport pathway shown in Figure 3l, which shows electron transfer from MoS_2 energy levels to the ITO electrode. The Fermi level of the illuminated heterojunction depends on which TMD in the heterojunction is photoexcited. In this case, the Fermi level of the heterojunction under MoS_2-selective excitation conditions is equivalent to isolated MoS_2 even though the photoexcited MoS_2 in the heterojunction is electronically and physically coupled to WS_2 (and even physically separated from the ITO electrode by WS_2). We attribute this observation to the fact that the heterojunction energy bands are a superposition of the monolayer energy states and are localized on different monolayers.[58] Photoexcited majority carriers reside in conduction band energy states that are MoS_2-like rather than mixed conduction band levels, whose energy level positions are different than the isolated monolayers. This wavelength-dependent Fermi level behavior is independent of the stacking orientation of the heterojunction. The E_{on} value of the ITO/MoS_2/WS_2 configuration under 650 nm illumination conditions is nearly equivalent to that of ITO/MoS_2 (Figure 5b). This observation further suggests that photogenerated carriers reside in MoS_2-like energy levels even though the TMDs are physically coupled. We conclude that E_{on} and, therefore, E_F of the illuminated heterojunction depend on which TMD is photoexcited.

In conclusion, we studied charge recombination and transport pathways as a function of stacking configuration and illumination conditions in MoS_2/WS_2 liquid junction photoelectrochemical cells. Photoluminescence microspectroscopy of ITO/MoS_2/WS_2 and ITO/WS_2/MoS_2 heterojunctions in air indicated efficient interlayer charge transfer, regardless of the heterojunction stacking configuration. Photoelectrochemical measurements of the same samples in iodide electrolytes showed distinct charge recombination and transport behavior. We observed a significant synergistic photocurrent enhancement effect upon exciting ITO/MoS_2/WS_2 electrodes with either 532 or 635 nm illumination. On the other hand, photoexcitation of the ITO/WS_2/MoS_2 sample with 532 nm illumination induces an interlayer recombination process, where electrons in MoS_2 recombine with holes in WS_2. This charge recombination pathway is active when both materials are photoexcited simultaneously and is mostly inactive under 635 nm illumination conditions that selectively excites MoS_2. This charge recombination pathway is significant for the development of bulk heterojunction (BH) TMD photoelectrodes made from randomly oriented TMD nanosheets.[19,60] BH electrodes exhibit random stacking configurations throughout the film, which could give rise to varying recombination pathways that depend on the carrier generation process, as we demonstrated herein. Finally, photogenerated carriers are transported as far as 3 μm along TMDs layers to reach a heterojunction interface. Charge transport simulations show that carriers diffuse along a concentration gradient from the focused laser sport to the heterojunction edge site. We envision that the knowledge gained in these heterojunctions can be used to develop efficient photoelectrocatalytic or solar energy conversion systems based on TMD heterojunctions.

■ ASSOCIATED CONTENT

Supporting Information

The Supporting Information is available free of charge at https://pubs.acs.org/doi/10.1021/acs.nanolett.9b04209.

> Detailed experimental methods; Raman maps; comparison of charge extraction pathways in solid-state and liquid junction devices; ensemble level electrochemical data; detailed photocurrent mapping and image analysis procedures; additional photocurrent maps; absorption spectra; excitation laser profiles; charge transport simulations; detailed *i-E* curve analysis (PDF)

■ AUTHOR INFORMATION

Corresponding Author

*E-mail: jsambur@colostate.edu.

ORCID

Li Wang: 0000-0002-5315-0593
Muhammad Tahir: 0000-0002-0986-293X
Justin B. Sambur: 0000-0002-8457-4946

Author Contributions

L.W. fabricated devices and performed experiments. M.T. and H.C. performed charge transport simulations. L.W. and J.B.S analyzed the data and wrote the manuscript.

Notes

The authors declare no competing financial interest.

■ ACKNOWLEDGMENTS

This material is based upon the work supported by the Air Force Office of Scientific Research under award no. FA9550-17-1-0255. M.T. and H.C. are supported by the startup funds of CSU.

DOI: 10.1021/acs.nanolett.9b04209
Nano Lett. 2019, 19, 9084−9094

REFERENCES

(1) Geim, A. K.; Grigorieva, I. V. Van der Waals heterostructures. *Nature* **2013**, *499*, 419.

(2) Novoselov, K. S.; Mishchenko, A.; Carvalho, A.; Castro Neto, A. H. 2D materials and van der Waals Heterostructures. *Science* **2016**, *353* (6298), aac9439.

(3) Duan, X.; Wang, C.; Pan, A.; Yu, R.; Duan, X. Two-Dimensional Transition Metal Dichalcogenides as Atomically Thin Semiconductors: Opportunities and Challenges. *Chem. Soc. Rev.* **2015**, *44* (24), 8859−8876.

(4) Liu, Y.; Weiss, N. O.; Duan, X.; Cheng, H.-C.; Huang, Y.; Duan, X. Van der Waals Heterostructures and Devices. *Nat. Rev. Mater.* **2016**, *1*, 16042.

(5) Cheng, R.; Li, D.; Zhou, H.; Wang, C.; Yin, A.; Jiang, S.; Liu, Y.; Chen, Y.; Huang, Y.; Duan, X. Electroluminescence and Photocurrent Generation from Atomically Sharp WSe_2/MoS_2 Heterojunction p−n Diodes. *Nano Lett.* **2014**, *14* (10), 5590−5597.

(6) Withers, F.; Del Pozo-Zamudio, O.; Mishchenko, A.; Rooney, A. P.; Gholinia, A.; Watanabe, K.; Taniguchi, T.; Haigh, S. J.; Geim, A. K.; Tartakovskii, A. I.; Novoselov, K. S. Light-emitting Diodes by Band-structure Engineering in van der Waals Heterostructures. *Nat. Mater.* **2015**, *14*, 301.

(7) Pu, J.; Takenobu, T. Monolayer Transition Metal Dichalcogenides as Light Sources. *Adv. Mater.* **2018**, *30* (33), 1707627.

(8) Koppens, F. H. L.; Mueller, T.; Avouris, P.; Ferrari, A. C.; Vitiello, M. S.; Polini, M. Photodetectors Based on Graphene, Other Two-Dimensional Materials and Hybrid Systems. *Nat. Nanotechnol.* **2014**, *9*, 780.

(9) Mak, K. F.; Shan, J. Photonics and Optoelectronics of 2D Semiconductor Transition Metal Dichalcogenides. *Nat. Photonics* **2016**, *10*, 216.

(10) Lee, C.-H.; Lee, G.-H.; van der Zande, A. M.; Chen, W.; Li, Y.; Han, M.; Cui, X.; Arefe, G.; Nuckolls, C.; Heinz, T. F.; Guo, J.; Hone, J.; Kim, P. Atomically Thin p−n Junctions with van der Waals Heterointerfaces. *Nat. Nanotechnol.* **2014**, *9*, 676.

(11) Li, C.; Cao, Q.; Wang, F.; Xiao, Y.; Li, Y.; Delaunay, J.-J.; Zhu, H. Engineering Graphene and TMDs Based van der Waals Heterostructures for Photovoltaic and Photoelectrochemical Solar Energy Conversion. *Chem. Soc. Rev.* **2018**, *47* (13), 4981−5037.

(12) Kang, J.; Tongay, S.; Zhou, J.; Li, J.; Wu, J. Band Offsets and Heterostructures of Two-Dimensional Semiconductors. *Appl. Phys. Lett.* **2013**, *102* (1), 012111.

(13) Furchi, M. M.; Höller, F.; Dobusch, L.; Polyushkin, D. K.; Schuler, S.; Mueller, T. Device Physics of van der Waals Heterojunction Solar Cells. *npj 2D Mater. Appl.* **2018**, *2* (1), 3.

(14) Furchi, M. M.; Pospischil, A.; Libisch, F.; Burgdörfer, J.; Mueller, T. Photovoltaic Effect in an Electrically Tunable van der Waals Heterojunction. *Nano Lett.* **2014**, *14* (8), 4785−4791.

(15) Wang, L.; Sambur, J. B. Efficient Ultrathin Liquid Junction Photovoltaics Based on Transition Metal Dichalcogenides. *Nano Lett.* **2019**, *19* (5), 2960−2967.

(16) Xu, S.; Li, D.; Wu, P. One-Pot, Facile, and Versatile Synthesis of Monolayer MoS_2/WS_2 Quantum Dots as Bioimaging Probes and Efficient Electrocatalysts for Hydrogen Evolution Reaction. *Adv. Funct. Mater.* **2015**, *25* (7), 1127−1136.

(17) Shi, J.; Tong, R.; Zhou, X.; Gong, Y.; Zhang, Z.; Ji, Q.; Zhang, Y.; Fang, Q.; Gu, L.; Wang, X.; Liu, Z.; Zhang, Y. Temperature-Mediated Selective Growth of MoS_2/WS_2 and WS_2/MoS_2 Vertical Stacks on Au Foils for Direct Photocatalytic Applications. *Adv. Mater.* **2016**, *28* (48), 10664−10672.

(18) Cai, Z.; Liu, B.; Zou, X.; Cheng, H.-M. Chemical Vapor Deposition Growth and Applications of Two-Dimensional Materials and Their Heterostructures. *Chem. Rev.* **2018**, *118* (13), 6091−6133.

(19) Pesci, F. M.; Sokolikova, M. S.; Grotta, C.; Sherrell, P. C.; Reale, F.; Sharda, K.; Ni, N.; Palczynski, P.; Mattevi, C. MoS_2/WS_2 Heterojunction for Photoelectrochemical Water Oxidation. *ACS Catal.* **2017**, *7* (8), 4990−4998.

(20) Sherrell, P. C.; Palczynski, P.; Sokolikova, M. S.; Reale, F.; Pesci, F. M.; Och, M.; Mattevi, C. Large-Area CVD MoS_2/WS_2 Heterojunctions as a Photoelectrocatalyst for Salt-Water Oxidation. *ACS Appl. Energy Mater.* **2019**, *2* (8), 5877−5882.

(21) Wu, J.; Lan, Z.; Lin, J.; Huang, M.; Huang, Y.; Fan, L.; Luo, G.; Lin, Y.; Xie, Y.; Wei, Y. Counter Electrodes in Dye-Sensitized Solar Cells. *Chem. Soc. Rev.* **2017**, *46* (19), 5975−6023.

(22) Hussain, S.; Patil, S. A.; Memon, A. A.; Vikraman, D.; Abbas, H. G.; Jeong, S. H.; Kim, H.-S.; Kim, H.-S.; Jung, J. Development of a $WS_2/MoTe_2$ Heterostructure as a Counter Electrode for the Improved Performance in Dye-Sensitized Solar Cells. *Inorg. Chem. Front.* **2018**, *5* (12), 3178−3183.

(23) Vikraman, D.; Arbab, A. A.; Hussain, S.; Shrestha, N. K.; Jeong, S. H.; Jung, J.; Patil, S. A.; Kim, H.-S. Design of WSe_2/MoS_2 Heterostructures as the Counter Electrode to Replace Pt for Dye-Sensitized Solar Cell. *ACS Sustainable Chem. Eng.* **2019**, *7* (15), 13195−13205.

(24) Yu, X.; Prévot, M. S.; Guijarro, N.; Sivula, K. Self-Assembled 2D WSe_2 Thin Films for Photoelectrochemical Hydrogen Production. *Nat. Commun.* **2015**, *6*, 7596.

(25) Voiry, D.; Yang, J.; Chhowalla, M. Recent Strategies for Improving the Catalytic Activity of 2D TMD Nanosheets Toward the Hydrogen Evolution Reaction. *Adv. Mater.* **2016**, *28* (29), 6197−6206.

(26) Faraji, M.; Yousefi, M.; Yousefzadeh, S.; Zirak, M.; Naseri, N.; Jeon, T. H.; Choi, W.; Moshfegh, A. Z. Two-Dimensional Materials in Semiconductor Photoelectrocatalytic Systems for Water Splitting. *Energy Environ. Sci.* **2019**, *12* (1), 59−95.

(27) Baugher, B. W. H.; Churchill, H. O. H.; Yang, Y.; Jarillo-Herrero, P. Optoelectronic Devices Based on Electrically Tunable p−n Diodes in a Monolayer Dichalcogenide. *Nat. Nanotechnol.* **2014**, *9*, 262.

(28) Pospischil, A.; Furchi, M. M.; Mueller, T. Solar-Energy Conversion and Light Emission in an Atomic Monolayer p−n Diode. *Nat. Nanotechnol.* **2014**, *9*, 257.

(29) Hong, X.; Kim, J.; Shi, S.-F.; Zhang, Y.; Jin, C.; Sun, Y.; Tongay, S.; Wu, J.; Zhang, Y.; Wang, F. Ultrafast Charge Transfer in Atomically Thin MoS_2/WS_2 Heterostructures. *Nat. Nanotechnol.* **2014**, *9*, 682.

(30) Chen, H.; Wen, X.; Zhang, J.; Wu, T.; Gong, Y.; Zhang, X.; Yuan, J.; Yi, C.; Lou, J.; Ajayan, P. M.; Zhuang, W.; Zhang, G.; Zheng, J. Ultrafast Formation of Interlayer Hot Excitons in Atomically Thin MoS_2/WS_2 Heterostructures. *Nat. Commun.* **2016**, *7*, 12512.

(31) Ceballos, F.; Ju, M.-G.; Lane, S. D.; Zeng, X. C.; Zhao, H. Highly Efficient and Anomalous Charge Transfer in van der Waals Trilayer Semiconductors. *Nano Lett.* **2017**, *17* (3), 1623−1628.

(32) Ji, Z.; Hong, H.; Zhang, J.; Zhang, Q.; Huang, W.; Cao, T.; Qiao, R.; Liu, C.; Liang, J.; Jin, C.; Jiao, L.; Shi, K.; Meng, S.; Liu, K. Robust Stacking-Independent Ultrafast Charge Transfer in MoS_2/WS_2 Bilayers. *ACS Nano* **2017**, *11* (12), 12020−12026.

(33) Jin, C.; Ma, E. Y.; Karni, O.; Regan, E. C.; Wang, F.; Heinz, T. F. Ultrafast Dynamics in van der Waals Heterostructures. *Nat. Nanotechnol.* **2018**, *13* (11), 994−1003.

(34) Kozawa, D.; Carvalho, A.; Verzhbitskiy, I.; Giustiniano, F.; Miyauchi, Y.; Mouri, S.; Castro Neto, A. H.; Matsuda, K.; Eda, G. Evidence for Fast Interlayer Energy Transfer in $MoSe_2/WS_2$ Heterostructures. *Nano Lett.* **2016**, *16* (7), 4087−4093.

(35) Kline, G.; Kam, K.; Canfield, D.; Parkinson, B. A. Efficient and Stable Photoelectrochemical Cells Constructed with WSe_2 and $MoSe_2$ Photoanodes. *Sol. Energy Mater.* **1981**, *4* (3), 301−308.

(36) Tenne, R.; Wold, A. Passivation of Recombination Centers in n-WSe_2 Yields High Efficiency (>14%) Photoelectrochemical Cell. *Appl. Phys. Lett.* **1985**, *47* (7), 707−709.

(37) Lin, Y.-C.; Zhang, W.; Huang, J.-K.; Liu, K.-K.; Lee, Y.-H.; Liang, C.-T.; Chu, C.-W.; Li, L.-J. Wafer-Scale MoS_2 Thin Layers Prepared by MoO_3 Sulfurization. *Nanoscale* **2012**, *4* (20), 6637−6641.

(38) Lee, C.; Yan, H.; Brus, L. E.; Heinz, T. F.; Hone, J.; Ryu, S. Anomalous Lattice Vibrations of Single- and Few-Layer MoS_2. *ACS Nano* **2010**, *4* (5), 2695−2700.

DOI: 10.1021/acs.nanolett.9b04209
Nano Lett. 2019, 19, 9084−9094

(39) Li, X.-L.; Han, W.-P.; Wu, J.-B.; Qiao, X.-F.; Zhang, J.; Tan, P.-H. Layer-Number Dependent Optical Properties of 2D Materials and Their Application for Thickness Determination. *Adv. Funct. Mater.* **2017**, *27* (19), 1604468.
(40) Steinhoff, A.; Kim, J. H.; Jahnke, F.; Rösner, M.; Kim, D. S.; Lee, C.; Han, G. H.; Jeong, M. S.; Wehling, T. O.; Gies, C. Efficient Excitonic Photoluminescence in Direct and Indirect Band Gap Monolayer MoS_2. *Nano Lett.* **2015**, *15* (10), 6841−6847.
(41) Zhang, J.; Hong, H.; Lian, C.; Ma, W.; Xu, X.; Zhou, X.; Fu, H.; Liu, K.; Meng, S. Interlayer-State-Coupling Dependent Ultrafast Charge Transfer in MoS_2/WS_2 Bilayers. *Adv. Sci.* **2017**, *4* (9), 1700086.
(42) Li, L.; Long, R.; Prezhdo, O. V. Charge Separation and Recombination in Two-Dimensional MoS_2/WS_2: Time-Domain ab Initio Modeling. *Chem. Mater.* **2017**, *29* (6), 2466−2473.
(43) Tongay, S.; Fan, W.; Kang, J.; Park, J.; Koldemir, U.; Suh, J.; Narang, D. S.; Liu, K.; Ji, J.; Li, J.; Sinclair, R.; Wu, J. Tuning Interlayer Coupling in Large-Area Heterostructures with CVD-Grown MoS_2 and WS_2 Monolayers. *Nano Lett.* **2014**, *14* (6), 3185−3190.
(44) Wang, L.; Schmid, M.; Nilsson, Z. N.; Tahir, M.; Chen, H.; Sambur, J. B. Laser Annealing Improves the Photoelectrochemical Activity of Ultrathin $MoSe_2$ Photoelectrodes. *ACS Appl. Mater. Interfaces* **2019**, *11* (21), 19207−19217.
(45) Dotan, H.; Sivula, K.; Grätzel, M.; Rothschild, A.; Warren, S. C. Probing the Photoelectrochemical Properties of Hematite (α-Fe_2O_3) Electrodes Using Hydrogen Peroxide as a Hole Scavenger. *Energy Environ. Sci.* **2011**, *4* (3), 958−964.
(46) Hill, H. M.; Rigosi, A. F.; Rim, K. T.; Flynn, G. W.; Heinz, T. F. Band Alignment in MoS_2/WS_2 Transition Metal Dichalcogenide Heterostructures Probed by Scanning Tunneling Microscopy and Spectroscopy. *Nano Lett.* **2016**, *16* (8), 4831−4837.
(47) Kam, K. K.; Parkinson, B. A. Detailed Photocurrent Spectroscopy of the Semiconducting Group VIB Transition Metal Dichalcogenides. *J. Phys. Chem.* **1982**, *86* (4), 463−467.
(48) Lewerenz, H. J.; Gerischer, H.; Lübke, M. Photoelectrochemistry of WSe_2 Electrodes: Comparison of Stepped and Smooth Surfaces. *J. Electrochem. Soc.* **1984**, *131* (1), 100−104.
(49) Howell, S. L.; Jariwala, D.; Wu, C.-C.; Chen, K.-S.; Sangwan, V. K.; Kang, J.; Marks, T. J.; Hersam, M. C.; Lauhon, L. J. Investigation of Band-Offsets at Monolayer−Multilayer MoS_2 Junctions by Scanning Photocurrent Microscopy. *Nano Lett.* **2015**, *15* (4), 2278−2284.
(50) Chen, K.; Wan, X.; Wen, J.; Xie, W.; Kang, Z.; Zeng, X.; Chen, H.; Xu, J.-B. Electronic Properties of MoS_2−WS_2 Heterostructures Synthesized with Two-Step Lateral Epitaxial Strategy. *ACS Nano* **2015**, *9* (10), 9868−9876.
(51) Wu, W.; Zhang, Q.; Zhou, X.; Li, L.; Su, J.; Wang, F.; Zhai, T. Self-Powered Photovoltaic Photodetector Established on Lateral Monolayer MoS_2-WS_2 Heterostructures. *Nano Energy* **2018**, *51*, 45−53.
(52) Ceballos, F.; Zhao, H. Ultrafast Laser Spectroscopy of Two-Dimensional Materials Beyond Graphene. *Adv. Funct. Mater.* **2017**, *27* (19), 1604509.
(53) Bolts, J. M.; Wrighton, M. S. Correlation of Photocurrent-Voltage Curves with Flat-Band Potential for Stable Photoelectrodes for the Photoelectrolysis of Water. *J. Phys. Chem.* **1976**, *80* (24), 2641−2645.
(54) Cooper, G.; Turner, J. A.; Nozik, A. J. Mott-Schottky Plots and Flatband Potentials for Single Crystal Rutile Electrodes. *J. Electrochem. Soc.* **1982**, *129* (9), 1973−1977.
(55) Grätzel, M. Photoelectrochemical cells. *Nature* **2001**, *414* (6861), 338−344.
(56) Walter, M. G.; Warren, E. L.; McKone, J. R.; Boettcher, S. W.; Mi, Q.; Santori, E. A.; Lewis, N. S. Solar Water Splitting Cells. *Chem. Rev.* **2010**, *110* (11), 6446−6473.
(57) Peter, L. M. Dynamic Aspects of Semiconductor Photoelectrochemistry. *Chem. Rev.* **1990**, *90* (5), 753−769.
(58) Kośmider, K.; Fernández-Rossier, J. Electronic Properties of the MoS_2-WS_2 Heterojunction. *Phys. Rev. B: Condens. Matter Mater. Phys.* **2013**, *87* (7), 075451.
(59) Gong, C.; Zhang, H.; Wang, W.; Colombo, L.; Wallace, R. M.; Cho, K. Band Alignment of Two-Dimensional Transition Metal Dichalcogenides: Application in Tunnel Field Effect Transistors. *Appl. Phys. Lett.* **2013**, *103* (5), 053513.
(60) Su, T.; Shao, Q.; Qin, Z.; Guo, Z.; Wu, Z. Role of Interfaces in Two-Dimensional Photocatalyst for Water Splitting. *ACS Catal.* **2018**, *8* (3), 2253−2276.

DOI: 10.1021/acs.nanolett.9b04209
Nano Lett. 2019, 19, 9084−9094